

3D Cloud Detection and Tracking for Solar Forecast using Multiple Sky Imagers

Zhenzhou Peng
Dept. of Electrical & Computer Engineering
Stony Brook University
zhenzhou.peng@stonybrook.edu

Shinjaee Yoo, Dantong Yu
Computational Science Center
Brookhaven National Laboratory
{sjyoo, dtu}@bnl.gov

Dong Huang, Paul Kalb, John Heiser
Environmental Sciences Department
Brookhaven National Lab.
{dhuang, kalb, heiser}@bnl.gov

ABSTRACT

Cloud detection and tracking (CDT) is the most challenging problem in integrating solar energy into the smart grid. In this paper, we present a novel 3D cloud detection and tracking using images from three TSI (Total Sky Imager), and propose to incorporate history into a multi-layer cloud detection pipeline. Our pilot study shows that the new CDT significantly improves the short-term solar irradiance forecasting and enable regional radiation prediction, which is impossible with a single TSI.

Categories and Subject Descriptors

H.4 [Information Systems Applications]: Miscellaneous; D.2.8 [Software Engineering]: Metrics—complexity measures, performance measures

General Terms

System and Algorithm

Keywords

cloud tracking, cloud detection, SmartGrid

1. INTRODUCTION

Cloud is the primary source of solar radiation fluctuation. By blocking and diffusing sunlight, clouds show different optical properties in visible spectrum, and affect gross radiation collected by surface radiation sensors. Such variability is one of the biggest concern in power grid given the rapid increase of solar energy penetration in the electric grid. On the other hand, cloud field and its movement can be clearly recorded. The captured data can be used to predict the solar irradiation level, mitigate energy fluctuation and thereby stabilize the electric power grid. Therefore, the accurate

Permission to make digital or hard copies of all or part of this work for personal or classroom use is granted without fee provided that copies are not made or distributed for profit or commercial advantage and that copies bear this notice and the full citation on the first page. To copy otherwise, to republish, to post on servers or to redistribute to lists, requires prior specific permission and/or a fee.

SAC'14 March 24-28, 2014, Gyeongju, Korea.

Copyright 2014 ACM 978-1-4503-2469-4/14/03 ...\$15.00.

<http://dx.doi.org/10.1145/2554850.2554913>

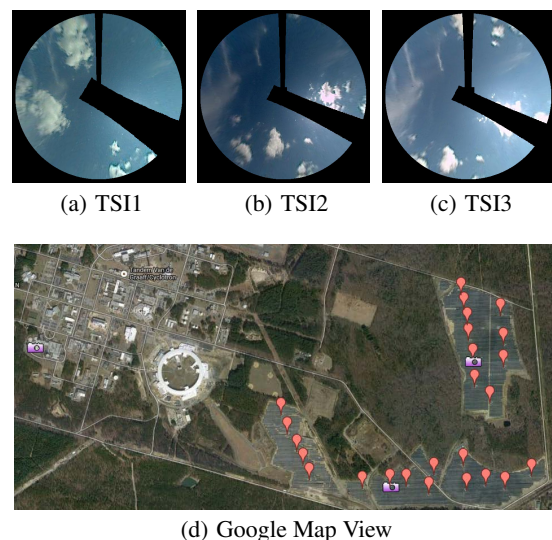


Figure 1: (a), (b), (c) are views of 3 TSIs. Black area is shadowband and image boundary removed in preprocessing. (d) is Google Map view of TSI1,2,3 from left to right (camera label) and 25 solar radiation sensors (red).

solar irradiance prediction by detecting and tracking clouds is an important and urgent problem in smart grid integration.

To date, previous works for cloud detection and tracking (CDT) are constrained by the complexity of cloud tracking or expensive tracking devices. The majority of research works focus on a large scale tracking using remote sensing techniques[2] [8]. But the quality of cloud movements detection and tracking is of low accuracy, especially in mesoscale with low temporal (30 minutes to hours) and spacial resolution (1x1Km or lower). For local scale applications such as distributed roof-top solar panels, cloud tracking requires much higher resolution in term of meters and seconds due to the volatility of weather and atmosphere condition within such time and spatial resolutions. Localized tracking is challenging as cloud has unpredictable properties of: 1) multi-layered distribution (heights ranging from 500m to 20000m), 2) the formation and deformation of cloud shape, and 3) ambiguous cloud boundaries depending on cloud types. Another issue of cloud tracking is the expensive cost of meteorologic instruments, like LIDAR and

cloud-resolving radar. To make cloud tracking more cost-effective, recently Huang et al. [4] proposed to detect multi-layer clouds and estimated cloud motion using TSI (Total Sky Imager) to address the aforementioned concerns. The TSI camera captures cloud visually (Figure 1) and takes a hemispheric snapshot of sky by the reflection of its dome-shape mirror on every 10 seconds. However, the previous work has several limitations: 1) no cloud boundary detection algorithm, 2) no vertical height distribution derived, 3) large motion estimation error due to no height and boundary information, and 4) limited view ranges and therefore quite short prediction ability with a single TSI.

To address these concerns, we propose to use multiple TSI imagers to detect the 3D layout of clouds. 3D reconstruction requires clear cloud boundary detection, cloud height estimation, and image stitching to fill the shadowband and holding arm which are designed to protect camera from direct-normal sunlight. The benefits of 3D reconstruction includes: 1) Cloud height information to correlate or predict solar radiation that are near, but not co-located with TSI devices, a.k.a. regional radiation prediction for the vicinity of TSIs. 2) Accurate image filling for shadowband and holding arm, and 3) bigger view ranges or longer time prediction abilities in comparison to a single TSI.

We deployed three TSIs in multiple geographic locations to reconstruct cloud in a 3D space. Figure 1 shows the deployed TSI locations and 25 solar radiation sensors located in the Long Island Solar Farm (LISF) to verify our irradiance prediction.

Our approach is based on computational geometry and machine learning. To estimate the height of cloud, we use TSI network to locate overlapped image areas that can derive the heights of clouds. To stitch images together, we proposed a cloud detection algorithm. Since there might exist noise in TSI images and errors in the pre-processing pipeline, we designed our algorithm to be robust. Based on the stitched images, we provided several radiation prediction models to show the effectiveness of our 3D cloud detection and tracking method. Our summarized contributions are as follows:

1. **Introducing 3D CDT (Cloud Detection and Tracking):** To the best of our knowledge, nobody has been applied multiple TSI networks to get the height information and track cloud in the Smart Grid application area. It is an important and effective methodology for a short term solar irradiance prediction.
2. **Supervised Cloud Detection:** We propose a robust supervised cloud detection algorithm that can select multiple robust features to stably predict cloud area and subsequently improve the quality of image processing using the detected boundaries.
3. **Robust Cloud Tracking Algorithm:** We propose a novel multi-camera and multi-frame based cloud tracking algorithm. Each TSI itself and its generated individual frames are limited by various artifacts, and might produce abnormal results. However, by taking both multiple TSIs and image history into consideration, we could design much more robust tracking algorithm to uncover the cloud properties accurately, for example cloud height estimation.
4. **Wind Field Detection:** With new cloud tracking algorithm, we detect wind fields and their associated height information. The wind field information helps us to identify cloud motion and layers, therefore significantly improve the quality of future cloud location.
5. **Irradiance Forecast:** We build four prediction models in comparison with persistent model based on 25 solar sensors' measurement. Our pilot analysis confirms the proposed 3D CDT and predication models could successfully forecast up to three minutes with high confidence.

2. CLOUD DETECTION

Tracking clouds on multiple TSI images requires accurate cloud

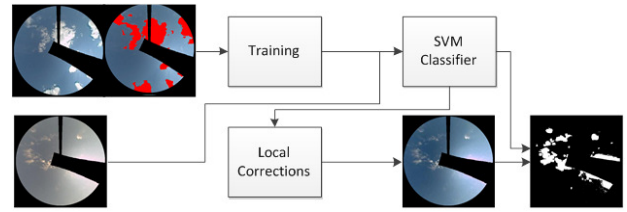


Figure 2: SVM cloud detector with local corrections

detection for various cloud properties. However, there are challenges on cloud detection:

1. **Brightness changes.** For different seasons and days, even within a single day, image color and contrast can vary due to the changing intensity of sunlight and atmospheric circumstances. Especially on TSI images, the partial blocked sunlight by shadowband may bring noise and lead to unstable color contrast.
2. **Various optical properties.** Clouds have different brightness and colors due to various particle distributions. Some of them have similar color pattern compared to sky, such as cirrus cloud.
3. **Non-rigid edge.** Since cloud is in arbitrary shape and edge, cloud detection is difficult, especially near blurry boundaries. Various existing derivative descriptor approaches are not robust.
4. **Unsupervised vs. Supervised.** For unsupervised methods, cloud detection can be constrained by an image segmentation which suffers from non-rigid edge. In the case of supervised methods, it is difficult to manually label cloud pixels on many images for both inside and boundaries of clouds.

To resolve these issues, a robust supervised classifier is required with less sensitive features. Furthermore, we also propose to improve classification quality based on cloud detection results and to enhance image contrast and equalize image histograms.

As shown in Figure 2, after manually labeling cloud area on an image, we design a supervised classifier using Support Vector Machine (SVM) [6]. SVM is based on a max-margin hyperplane principle to decrease the error and outlier effect and provides non-linear classification using kernel trick. We extract basic R,G,B values and calculate two additional features, Red Blue Ratio (RBR) and Laplacian of Gaussian (LoG) [1] from the training data. RBR emphasizes the intuitive knowledge that sky is more blue than cloud pixel. In fact, RBR has been proven to be effective in calculating cloud fraction based TSI images as well in related work [7]. LoG spatial filter is able to find the local minima/maxima color changes and provides the boundary information especially around the ambiguous cloud edges.

To further improve image quality, we use the cloud classification results to perform standard deviation correction and image histogram equalization. Since three TSIs have overlaps in their covered sky areas, the color histogram distribution, cloud optical properties, and associated cloud patterns should be similar at the same timestamp. Specifically, sky/cloud pixels detected by the SVM classifier are used to find the standard deviation of luminance and the RGB histogram as the cloud patterns. Based on these patterns, original images with low quality are adjusted to enhance contrast to make the rest of pipeline work better.

To test robustness under different cloud conditions and optical properties, we select various test cases: overcast, cloudy, multi-layer with distinctive patterns (Figure 3(a), 3(b), 3(c)). Cloud detection results for different cloud conditions have good quality except for multi-layer cloud near the Sun's position inside the shadowband. With multiple TSIs, the false cloud area can be ignored because no motion vectors can be detected (Section 3). Since the

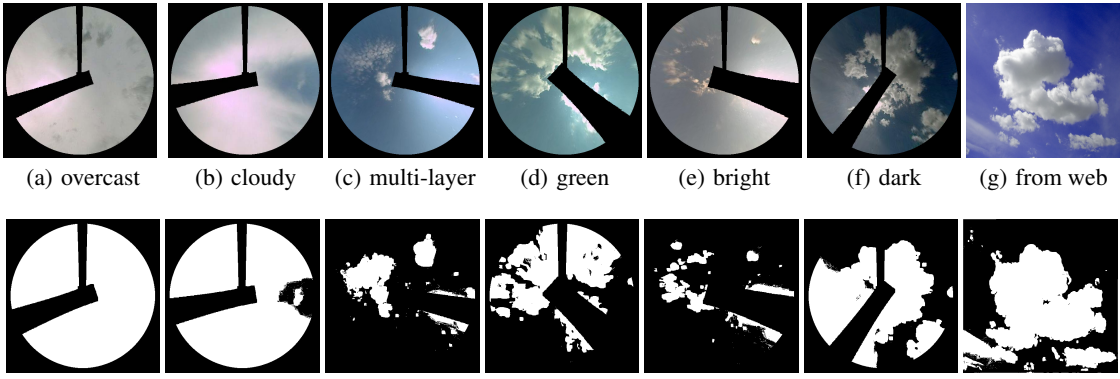


Figure 3: Cloud classifier performance test. (a), (b) and (c) have different atmospheric conditions compared with training data. (d), (e) and (f) have abnormal RGB scale due to exposure problem. (g) is a test image from web.

color scale of TSI fluctuates with the sunlight intensity, we choose three unusual test cases, each of which has the problem of green-dominant, over-exposure, and low-exposure respectively (Figure 3(d) 3(e) 3(f)). We also test cloud detector on an image from Web which is different with regard to the view range and color scale (Figure 3(g)), confirming that our cloud detection is practical and effective beyond TSI images.

3. CLOUD TRACKING

Previous works for cloud tracking [4][5] made use of only a single TSI with one sequence of source images or attempt to use the images from two individual TSIs. Image analysis on one TSI is independent to the other TSI. Here we design a new algorithm that integrates both temporal information of image sequences evolving over time and spatial information of multiple TSIs together to improve the quality of cloud tracking and detect wind fields based on the newly acquired/extracted the cloud height information.

3.1 Affine Transformation Model

In three TSI network, 3D cloud detection and tracking require an affine transformation model to define a mapping between spatial coordinate and image pixels so as to track clouds on 2D images. we can simplify 3D affine model under two assumptions: 1) clouds only have planar motion vectors. In other words, motion vectors retain the movement within the same height level, which is sufficient for the solar irradiance prediction application. In our approach, our focus is to find short-term sunlight blocked by clouds instead to track vertical cloud shifts. 2) All TSIs have the same view range, focal specifications, and are leveled to have the same upward view angle. The deployed three TSIs use the same cameras and adjust their view range facing straight up. With the above two assumptions, 2D representations of 3D motion vectors are identical among multiple TSIs while affine transformation of objects between any pair of TSIs is only pixel shifting without rotation, scaling and shearing.

3.2 Motion and Displacement Detection

Based on the affine transformation, cloud tracking contains two components: motion tracking(temporal) and height estimation(spacial). In case of temporal tracking, if a pixel value with a coordinate $\mathbf{c} = \langle x, y \rangle$ on TSI i is $I_i^t(\mathbf{c})$ at frame t , then a motion vector $\mathbf{v}^t = \langle v_1, v_2 \rangle$ at time t is defined as follows:

$$I_i^{t+1}(\mathbf{c}) = I_i^t(\mathbf{c} + \mathbf{v}^t) = I_i^t(\langle x + v_1, y + v_2 \rangle) \quad (1)$$

In practice, we consider a block of pixels as the unit of any movement. Thereby \mathbf{c} stands for the centre of a cloud block and \mathbf{v}^t is the block movement between t and $t + 1$. In case of spacial aspect (displacement vector among TSIs), identifying overlapping cloud regions between a pair of TSI images leads to cloud height estimation, an essential property for cloud tracking. With the height information, we can easily calculate actual cloud speed and the mapping between each image pixel to its corresponding ground surface coordinate. Suppose the same cloud region has a displacement $\mathbf{d}^{i,j,t}$ between TSI i and j at time t , then $\mathbf{d}^{i,j,t} = \langle d_1, d_2 \rangle$ is defined as follows:

$$I_i^t(\mathbf{c}) = I_j^t(\mathbf{c} + \mathbf{d}^{i,j,t}) \quad (2)$$

Given three TSI sites ($S = \{1, 2, 3\}$) with consecutive frames (t and next $t + 1$), the objective function φ for cloud tracking is to maximize correlations among TSI sites and consistency across history, which can be defined as follows:

$$\begin{aligned} \underset{\mathbf{d}^{i,j,t}, \mathbf{v}^t}{\operatorname{argmax}} \quad \varphi(\mathbf{c}, t, S) = & \sum_{i,j \in S, i \neq j} NCC(I_i^t, I_j^t, \mathbf{c}, \mathbf{d}^{i,j,t}) \\ & + \sum_{i \in S} NCC(I_i^t, I_i^{t+1}, \mathbf{c}, \mathbf{v}^t) \end{aligned} \quad (3)$$

where NCC is a normalized cross correlation between two image blocks. The following Equation defines NCC :

$$\begin{aligned} NCC(I, J, \mathbf{c}, \mathbf{u}) = & \frac{1}{s} \sum_{\mathbf{k} = \langle i, j \rangle} \frac{(I(\mathbf{c} + \mathbf{k}) - \mu(I, \mathbf{c})) (J(\mathbf{c} + \mathbf{u} + \mathbf{k}) - \mu(J, \mathbf{c} + \mathbf{u}))}{\sigma(I, \mathbf{c}) \sigma(J, \mathbf{c} + \mathbf{u})} \end{aligned} \quad (4)$$

where I and J are image frames, \mathbf{u} is a movement or displacement vector, $i, j \in \{-n, -n + 1, \dots, 0, \dots, n\}$ are the index of image block, $s = (2n + 1)^2$ is a normalization constant, μ is a mean function, and σ is a standard deviation function for the image block. NCC is widely used in satellite cloud motion detections and image processing due to its simplicity and robustness of noise and intensity change.

Equation 3 for block searching is used on six image frames of three TSIs. If we do a brute-force search for $\mathbf{d}^{i,j,t}$, we need to try every possible locations. Such a search is extremely slow because a single NCC calculation is $O(n^2)$ for $n \times n$ image subblocks and a single TSI motion or displacement vector search is $O(n^2 m^2)$ with a $m \times m$ searching window where $m > n$. For k sites or TSIs, Equation 3 is $O(k^2 n^2 m^2)$ for $k(k - 1)/2$ displacement vectors plus $O(kn^2 m^2)$ for searching motion vectors.

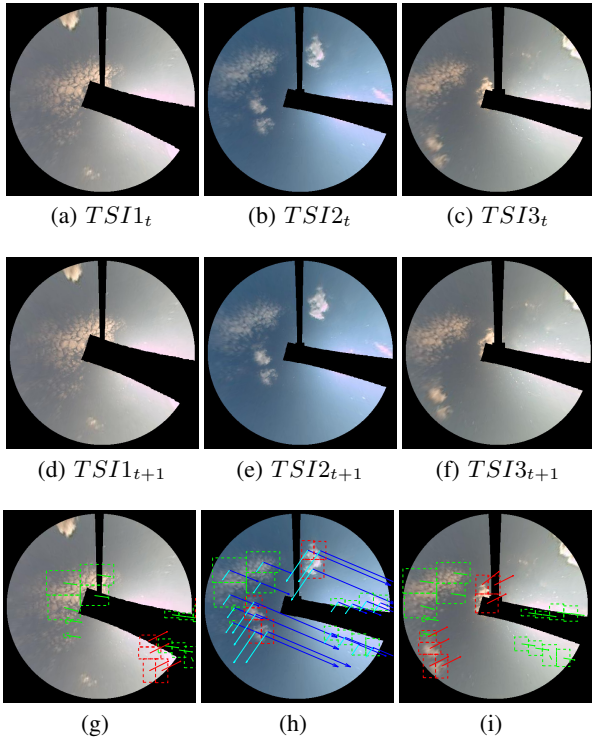


Figure 4: Cloud tracking on six images. Green blocks stand for wind field with altitude $h=3700\text{m}$ while red blocks indicate $h=1100\text{m}$. On (h), the displacement vectors from TSI2 to TSI3 are marked as blue while those for TSI2 to TSI1 are cyan. Motion vectors of each cloud block is plotted as green or red on (g) and (i), the same color as their associated cloud layer

Because three cameras are located close to each other and have overlapped view space, the computing time for displacement vectors can be reduced to only $O(k^2 n^2 h)$ where one TSI image pixel has the maximum of h possible corresponding positions on the other two TSI images, where $h < m$. In fact h is the range of altitudes that a pixel can be possibly associated with in a 3-D space. $\mathbf{d}^{i,j,t}$ between i and j does not need to be calculated if TSIs i and j are considerably far away. In our three TSI examples, we did not compute $\mathbf{d}^{1,3,t}$ since the distance between the first and third TSIs is large enough and they only have small overlapped view. Then the time complexity is $O(n^2 h)$.

Since TSI2 is in the middle geographically, cloud mask on TSI2's images extracted by cloud detector is segmented into small cloud blocks and then used for similarity searching individually. For instance, in Figure 4, assuming cloud tracking is based on two consecutive timestamps (t and $t+1$) with three TSIs, three layers of cloud are extracted as the solution of Equation 3. Around the shadowband dark area, high altitude cloud ($h=15000\text{m}$) is detected near the Sun spot. But there is no motion vector detected for this layer. So we treat it as over exposure noise. For the other two cloud layers ($h=1200$ and $h=3700$), their motion vectors point to the directions of two o'clock and four o'clock respectively.

3.3 Wind Field Detection

With temporal and spacial cloud tracking techniques, we design a wind field pipeline to integrate history information into current tracking. We define a wind field as a layer of clouds with the same height and no radical change among motion vector directions.

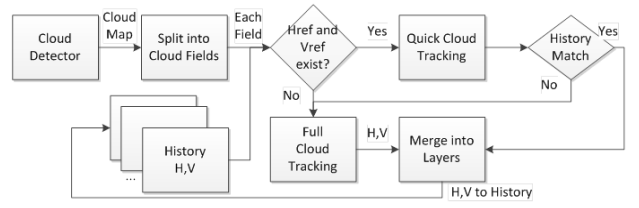


Figure 5: Pipeline of Multi-layer wind fields determination

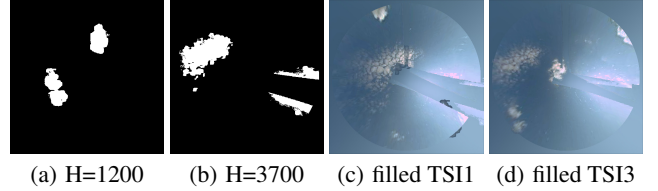


Figure 6: Image filling of two layers from Figure 4. TSI1 and TSI3 images are adjusted with histogram equalization and filled with default sky color if no cloud

Therefore, we can use historical wind fields as a prior knowledge of current cloud distribution. In our pipeline, we design two tracking models, matching against history and full search. In the case of history matching, cloud field is checked quickly in the layers detected in the previous tracking (historical wind fields). As for the full search, wind field assumes that motion vector can have any direction, scale and height level. In this case, wind field tracking is of no reference and solved by similarity optimization discussed in Section 3.2.

The schematic flowchart of wind field pipeline is shown in Figure 5. If a wind field is expressed in height and motion vector combination, $\langle h, \mathbf{v} \rangle$, n layers of wind fields can be presented as two collections: $H = \langle h_1, h_2, \dots, h_n \rangle$ and $V = \langle \mathbf{v}_1, \mathbf{v}_2, \dots, \mathbf{v}_n \rangle$. After cloud detection is completed, cloud area is divided into small blocks, assuming each of which has the same wind field with the same height. For each wind field, the historical layers for calculating the particular wind field are kept in collections of H_{ref} and V_{ref} . In experiment, we kept tracking of last ten consecutive frames of tracking results within 100 seconds. To locate each cloud field and find its layer information, we do similarity search in history collections H_{ref} and V_{ref} . If none of history layer is found to match current cloud block, then we treat the cloud field as a newly detected wind field and switch to full search mode to find $\langle h, \mathbf{v} \rangle$ for current cloud block. To remove the tracking noise, we choose up to three historical wind field layers.

In the end, we aggregate the tracking results of all cloud blocks for the current timestamp to get multiple layers of wind fields, H and V . The main reason for partitioning/merging cloud blocks based on wind field is to remove abnormality that happens in tracking within an individual wind field. The average height and motion vector of each layer are much more smooth and robust than that of individual cloud area even when texture noise and image distortion exist. For all detected layers, we record them in H_{ref} and V_{ref} .

The black area in TSI images stands for camera boundary or shadowband removed during the preprocessing step. Image stitching is carried out by filling black area with multi-layer cloud information. Using the result in Figure 4, the image from TSI2 at time t has two layers of wind fields shown in Figure 6(c) and 6(d). For each layer with a certain height h , the displacements of TSI2 \rightarrow TSI1 and TSI2 \rightarrow TSI3 are defined from the affine transfor-

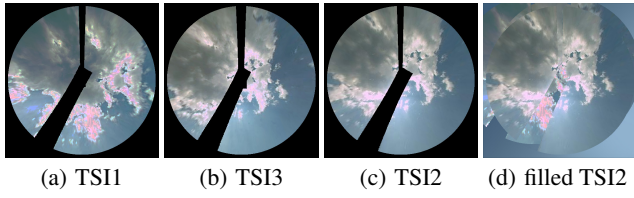


Figure 7: Fill missing part of (c) using (a) and (b) with reference to history layers.

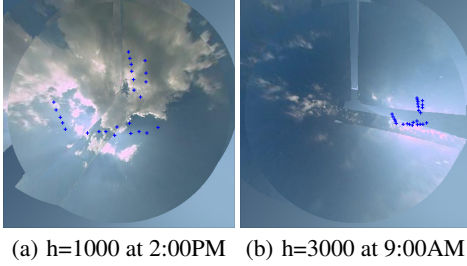


Figure 8: Corresponding pixels (Blue cross) of 25 solar panels on the filled TSI2 image at different height levels and local time

mation. Thereby, black areas on TSI1 and TSI3 can be filled by shifting TSI2 cloud pixels based on displacement vectors. For a multi-layer case, shift higher layer first since high altitude clouds may be blocked by lower layers. To make image stitching be more smooth, we use the mean value of sky color as the default filling color for the black area. The image stitching results between TSI1 and TSI3 are shown in Figure 6(c) and 6(d). By applying layers information, TSI2 image is recovered using TSI1 and TSI3 (Figure 7).

4. RADIATION PREDICTION MODELS

With stitched images using multi-layer wind fields, we can forecast solar irradiance level. Such a process requires two additional components: 1) estimating or locating the corresponding image pixel in the next (future) imageframe for each radiation sensor location and 2) building a prediction model.

To correlate radiation levels to TSI image pixels, we identify a sunlight blocking pixel for each wind field height. Our radiation value is calculated from the Global Horizontal Irradiance (GHI) index. The major factor to cause the GHI fluctuation is clouds along the sunlight traversing path. Given the wind field heights and cloud detection results, the corresponding pixel or sun-blocking pixel can be found by mapping the spatial coordinate to its projection on the TSI image. As illustrated in Figure 8, we show 25 sun-blocking pixels for all solar radiation sensors at two cloud height levels and local time. In order to predict solar irradiance value under the assumption of no radical change of cloud shape and motion within a short period of time, the locations of future corresponding pixels are estimated by moving current pixels based on extracted motion vectors for this layer. If multiple cloud layers exist, we choose a cloud pixel with the lowest cloud layer.

We build irradiance forecast models using the corresponding pixels from the predicted image frame of the next timestamp. Pixel-to-GHI problem can be formulated as $\hat{rad}^t = f(\mathbf{x}^t)$, where \hat{rad}^t stands for the estimated radiation at the time t and \mathbf{x}^t is the feature vector extracted from the correlated pixel. In our experiment, we choose 17 features to form the feature vector \mathbf{x}^t . To mitigate

noise and texture unstability, we use 3x3 window centered at the corresponding pixel to extract features. We take minimum, maximum, average value of R,G,B value within this window at the future timestamp t and the average values at the current timestamp $t - 1$. To avoid fluctuation of RGB color, we import RBR of centre pixel at t and $t - 1$ as input features. Other than features extracted from the corresponding window, the latest observed radiation value, rad^{t-1} , is added to stabilize the model and the cloud coverage at $t - 1$ is included to incorporate the diffused irradiance. We normalized GHI and 17 input features to range $[0,1]$.

In our study, we considered five different models from the simplest radiation shift model to the non-linear robust regression model. Our baseline **radiation shift**, *RShift*, is a persistent model which uses the observed radiation rad^{t-1} as the predicted radiation \hat{rad}^t .

$$\hat{rad}^t = rad^{t-1} \quad (5)$$

As an extension of baseline, we incorporate the cloud fluctuation represented by RBR change. The extended model is called **linear RBR delta** [3], *linear_δ*

$$\hat{rad}^t = rad^{t-1} + C \cdot (RBR^t - RBR^{t-1}) \quad (6)$$

where C is a negative coefficient for this linear relation. But other than RBR, *linear_δ* could not model other available features. To take all 17 attributes of x_t , we generalize *linear_δ* to an **ordinary linear regression model**, *linear*, to estimate a future radiation \hat{rad}^t :

$$\hat{rad}^t = \mathbf{w} \cdot \mathbf{x}^t + b \quad (7)$$

where \mathbf{w} is the weight vector and b is an intercept. However, the ordinary approach is sensitive to noise or outlier and suffers from the overfitting. To overcome these problems, we propose to apply **Support Vector Regression** (SVR). SVR is the regression version of Support Vector Machine. Given a linear kernel, a.k.a. *SVR_{linear}*, the radiation estimation follows a ordinary form in Equation 7 while the \mathbf{w}, b pair is obtained by solving classic SVR optimization problem:

$$\min_{\mathbf{w}, b, \xi, \xi^*} \frac{1}{2} \|\mathbf{w}\|^2 + C \sum_{i=1}^n (\xi_i + \xi_i^*) \quad (8)$$

subject to

$$\begin{aligned} (\mathbf{w} \cdot \mathbf{x}^t + b) - rad^t &\leq \varepsilon + \xi_i, \xi_i \geq 0, \forall i \\ (\mathbf{w} \cdot \mathbf{x}^t + b) - rad^t &\geq -\varepsilon - \xi_i^*, \xi_i^* \geq 0, \forall i \end{aligned} \quad (9)$$

where ε is the margin for regression, ξ_i and ξ_i^* are slack variables, and C is a regularization parameter. By incorporating different kernels, we can extend SVR to model non-linear relationship by projecting current attributes into high-dimensional feature spaces. We use the RBF (Radial Basis Function) kernel, *SVR_{rbf}*, with σ as RBF smoothing parameter:

$$\begin{aligned} \hat{rad}^t &= k(\mathbf{w}', \mathbf{x}^t) + b \\ k(\mathbf{w}', \mathbf{x}^t) &= \phi(\mathbf{w}') \cdot \phi(\mathbf{x}^t) = e^{-\frac{\|\mathbf{w}' - \mathbf{x}^t\|^2}{2\sigma^2}} \end{aligned} \quad (10)$$

5. RESULTS

To validate the effectiveness of our 3D cloud detection and tracking algorithms, we evaluate the performance of the prediction models that are based on tracking results. To set up experiment, we downloaded five hours data between 10:00AM and 15:00PM on 06/17/2013 from the LISF. On that day, there were up to three cloud layers and various cloud types from scattered cloud in the morning

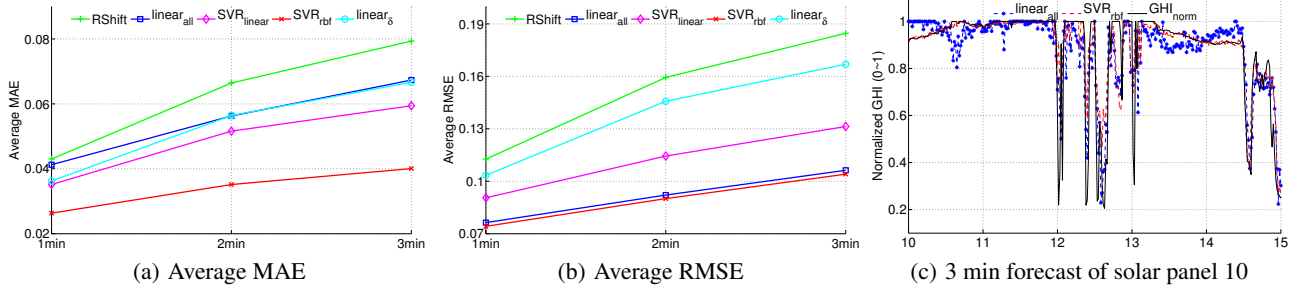


Figure 9: Solar irradiance prediction using 5 models. (a) and (b) are average MAE and RMSE score of 25 solar panels. (c) is 3-minute linear and SVR_{rbf} prediction output of solar panel 10 compared with ground-truth.

to overcast in afternoon. For the cloud tracking purpose, ten seconds data of three TSIs (total 5400 images) are used for motion and layer extraction. TSI2 images are subsequently filled with the aforementioned image stitching algorithm. To set up forecast models, corresponding pixels and GHI radiation per minute for 25 solar sensors are extracted and downloaded. Thereby 7500 records in total are used as training dataset. As in Section 4, we extract 17 input features \mathbf{x}^t to feed into forecast models. In case of overfitting in training, we use 5-fold cross validation. For both linear and non-linear SVR models, parameters including regularization weight C , error tolerance range ε and RBF smoothness factor σ , need to be tuned. In our experiment, we select optimal parameters in certain ranges. Here C is tuned in range $C = [-1024, 1024]$, while ε is from $\varepsilon = [0.001, 0.6]$ and σ is in range of $\sigma = [10^{-4}, 10^4]$. The average values of 25 solar sensors for SVR_{linear} are set to be $C_{avr} = 35, \varepsilon_{avr} = 0.01$. In the case of SVR_{rbf}, $C_{avr} = 19, \varepsilon_{avr} = 0.003, \sigma_{avr} = 0.2291$. For linear and linear_θ, training is based on the least square error scheme while persistent RShift needs no training.

To evaluate models' performance, we use Root Mean Square Error (RMSE) and Mean Absolute Error (MAE) to measure prediction error. The RMSE metric gives more weight on big errors which could be caused by wrong cloud condition estimations in the cloud tracking. In terms of MAE, it presents the average forecast error well. The forecast results up to three minutes are shown in Figure 5. The average RMSE and MAE values of 25 solar sensors are presented in Figure 9(a) and 9(b). Figure 9(c) shows an example of the forecast radiation sequence for solar panel 10, including three-minute prediction results of linear and SVR_{rbf}, and the ground-truth measurements. Our results show that all of our prediction models are much better than the baseline, RShift. But linear has bigger MAE error rate than linear_θ, which is consistent with the fact that linear model tends to minimize big errors excessively during its training step and does not perform well due to over fitting. Overall, our pipeline works well to capture irradiance changes. Compared to all linear models, SVR_{rbf} shows the best performance and least error rates in both evaluation metrics. Our cloud tracking algorithm produces much more features than before. Experiments show that the forecast models built on top of the tracking algorithm can take advantage of the newly acquired features, thereby are more robust than previous work and remain to be accurate even when the prediction time range increases.

6. CONCLUSION

In this paper, we proposed a novel 3D cloud detection and tracking algorithms using both computational geometry and machine learning methods, which not only improve the current state of the

art cloud detection and tracking results but also enable us to predict solar irradiance nearby sites or regional radiation prediction. It is solely possible by multiple TSIs, which bring the power to estimate cloud heights. We show the effectiveness of our new 3D cloud detection and tracking pipeline performance by showing irradiance prediction and all of our four proposed models significantly improved performance in both MAE and RMSE evaluation metrics.

7. ACKNOWLEDGMENT

This research is part of "A Public-Private-Academic Partnership to Advance Solar Power Forecasting". It is supported in part by DOE grants DE-AC02-98CH10886.

8. REFERENCES

- [1] B. E. Boser, I. M. Guyon, and V. N. Vapnik. A training algorithm for optimal margin classifiers. In *Proceedings of the fifth annual workshop on Computational learning theory*, pages 144–152. ACM, 1992.
- [2] H. Escrig, F. Batlles, J. Alonso, F. Baena, J. Bosch, I. Salbidegoitia, and J. Burgaleta. Cloud detection, classification and motion estimation using geostationary satellite imagery for cloud cover forecast. *Energy*, 2013.
- [3] H. Huang, J. Xu, Z. Peng, S. Yoo, D. Yu, D. Huang, and H. Qin. Cloud motion estimation for short term solar irradiance prediction. In *accepted by IEEE SmartGridComm Symposium 2013*, 2013.
- [4] H. Huang, S. Yoo, D. Yu, D. Huang, and H. Qin. Correlation and local feature based cloud motion estimation. In *Proceedings of the Twelfth International Workshop on Multimedia Data Mining*, pages 1–9. ACM, 2012.
- [5] E. Kassianov, C. N. Long, and J. Christy. Cloud-base-height estimation from paired ground-based hemispherical observations. *Journal of Applied Meteorology*, 44(8):1221–1233, 2005.
- [6] T. Lindeberg. Detecting salient blob-like image structures and their scales with a scale-space primal sketch: a method for focus-of-attention. *International Journal of Computer Vision*, 11(3):283–318, 1993.
- [7] C. Long, D. Slater, and T. P. Tooman. *Total sky imager model 880 status and testing results*. Pacific Northwest National Laboratory, 2001.
- [8] J. Schmetz, K. Holmlund, J. Hoffman, B. Strauss, B. Mason, V. Gaertner, A. Koch, and L. Van De Berg. Operational cloud-motion winds from meteosat infrared images. *Journal of Applied Meteorology*, 32(7):1206–1225, 1993.